Proton Intercalated 2D Magnetic Bilayer: Controlled Magnetic Phase Transition and Half-metallicity via Ferroelectric Switching

*Lei Zhang [1,2], Cheng Tang [1,2], Stefano Sanvito [3], Aijun Du [*1,2]*

[1] School of Chemistry and Physics, Queensland University of Technology, Gardens Point Campus, Brisbane, QLD 4000, Australia

[2] Centre for Materials Science, Queensland University of Technology, Gardens Point Campus, Brisbane, QLD 4000, Australia

[3]School of Physics and CRANN Institute, Trinity College, Dublin 2, Ireland

Abstract: Electrically controlled magnetism in two-dimensional (2D) multiferroics is highly desirable for both fundamental research and the future development of low-power nanodevices. Herein, inspired by the recently experimentally realized 2D antiferromagnetic $MnPSe_3$ [Ni, Z.; *Nat. Nanotechnol.* 2021, *16*, 782] and guided by a hetero-magnetic structural design, we engineer strong magneto-electric coupling in proton-intercalated 2D $MnPSe_3$ bilayer. Hydrogen functionalization breaks the centrosymmetry of bilayer $MnPSe_3$, leading to out-of-plane ferroelectricity. Moreover, there is a phase transition from antiferromagnetic semiconductor to ferromagnetic half-metal in the H-bonded $MnPSe_3$ layer, while the other remains antiferromagnetic and semiconducting. When reversing the electrical polarization the intercalated protons can flip between the top and bottom layer with an ultralow switching barrier. This allows one to tune the magnetic order and conductivity of the individual layers. Our results pave a new avenue to realize magnetoelectric coupling in single ferroic material. Furthermore, the ferroelectricity-controlled magnetic phase transition and half-metallicity offers promising application in spintronics.

The field of 2D magnetism is advancing rapidly,[1] and numerous atomic-thin magnetic materials have been experimentally realized, including ferromagnetic CrI_3,[2] $Cr_2(Si, Ge)_2Te_6$,[3, 4] and $V(Mn)Se_2$,[5, 6] and antiferromagnetic $MnPSe_3$.[7] The atomic thickness offers unique opportunities to explore the manipulation of the magnetic state via external perturbations like strain, pressure, light, charge doping, and electric field.[8-15] Of particular interest is the electrically controlled magnetic order, which not only addresses fundamental questions in exotic magnetic physics, but also may stimulate the advanced design of electrically coupled spintronics.[16] The switching between antiferromagnetic (AFM) and ferromagnetic (FM) order has been experimentally achieved in bilayer CrI_3,[12, 13] by means of a persistent electric field or electrostatic doping. Such transition relies on external stimuli and therefore it a volatile and energy-consuming process, a fact that poses great challenges to its future application in nonvolatile magnetoelectric nanodevices.

Multiferroic materials, displaying coexistence of ferroelectricity and magnetism, may offer an alternative opportunity to overcome such challenge, as the spontaneous electric polarization of a ferroelectric (FE) is nonvolatile.[17] However, due to the usual mutual exclusion of ferroelectricity and magnetism,[18] reports of 2D ferroelectric magnets are still rather limited.[19-23] Moreover, the two bistable polarized states of a typical ferroelectric material, +P and -P states, are in principle magnetic equivalent.[24] Namely, the +P and -P phases display the same magnetic order, seemingly excluding any possibility of achieving tunable magnetic orders through a ferroelectric transition. However, this limitation may be overcome in a multiferroic bilayer composed of one AFM and one FM layer, namely a hetero-magnetic structure. The +P state, with AFM upper layer and FM lower layer, and the -P state, with FM upper layer and AFM lower layer, are still degenerate, but the magnetic order of the individual layers can be switched by reversing the electrical polarization.

Inspired by recent experiments on the intercalation of hetero-atoms into van der Waals

materials,[25-30] here we report that the proton-intercalated $MnPSe_3$ bilayer provides an embodiment of such type of structural design. Due to the small atomic radii of hydrogen, the intercalated protons will only bind to one of the $MnPSe_3$ layers, leading to charge redistribution and Fermi level shift that turn the H-functionalized layer from AFM to FM halfmetallic. The AFM and semiconducting nature of pristine $MnPSe_3$ remains in the other layer, thus that the entire structure displays an AFM-FM hetero-magnetic order. Most interestingly, the biased lateral position of the intercalated protons also introduces out-of-plane polarity, whose direction can be switched at an ultralow energy barrier. Upon electrical polarization reversal,the intercalated proton detach from one layer and bind to the other. This achieves a long-sought nonvolatile FM/AFM and half-metallic/semiconducting transition.

Our density functional theory (DFT) calculations were carried out using the Vienna ab initio simulation package (VASP).[31-33] The projector augmented wave (PAW) method[34] was applied to describe the electron-core interaction. The exchange and correlation energy was treated with the generalized gradient approximation (GGA) parameterized by Perdew, Burke, and Ernzerhof (PBE) [35, 36]. The DFT-D3 scheme was applied to account for vdW interaction.[37] Considering the localized nature of the 3*d* electrons of Mn, the DFT+U method was applied with an effective *U*-*J* value of 5 eV in accordance with previous studies.[38] The cutoff energy for the plane-wave expansion was set to 400 eV and the *k*-points density was set to 0.025 2π/Å. The geometry was fully optimized until the residual forces and the energy were converged to 0.005 eV/Å and 1×10^{-6} eV, respectively. A vacuum region always larger than 15 Å was introduced to avoid the interaction between the neighboring periodic images. In addition to the PBE-GGA the Heyd-Scuseria-Ernzerhof hybrid functional (HSE06) was utilized to obtain accurate electronic structures and electric polarization.[39] The nudged elastic band (NEB) method [40] was employed to study the FE phase transition. Ab initio

molecular dynamics (AIMD) simulations were carried out for a total of 10 ps with a time step of 0.5 fs and an Andersen thermostat was applied to control the temperature.[41]

The $MnPSe_3$ bilayer (four formula units per unit cell) is most stable with an AB-stacking order similar to that of the bulk form (see Figure 1a).[42] Each monolayer contains two Mn atoms octahedrally coordinated by six Se atoms from the neighboring P_2Se_6 bipyramids. The two monolayers with Neel-type AFM spin texture are antiferromagnetically coupled to each other, giving a sizable vdW gap of 3.31 Å. This may facilitate the intercalation of protons. In order to determine the ground state of the proton-intercalated $MnPSe_3$ bilayer, various intercalating positions and magnetic configurations (shown in Figures 1b and c) are systematically scanned for several H_xMnPSe_3 (x = 1/4, 1/8, and 1/12) systems. The energy maps of H_xMnPSe_3 in different geometric and magnetic configurations are shown in Figure 2 and Figures S1-S3. Clearly, for all H_xMnPSe_3 prototypes considered in this work, the ground states always prefer an AB-stacking order with the proton bonded to the P site of one $MnPSe_3$ layer. The cohesive energy (E_{coh}), defined as $E_{coh} = [E_H + (E_{Mn} + E_P + 3E_{Se})/x - E_{tot}]/(1 + 5/x)$ where E_H, E_{Mn}, E_P, E_{Se}, and E_{tot} are the energies of a single H, Mn, P, Se atom and H_xMnPSe_3 bilayer system, respectively, is then calculated. We find E_{coh} as large as around 3.3 eV/atom, suggesting that the proton intercalated $MnPSe_3$ is highly thermodynamically feasible.

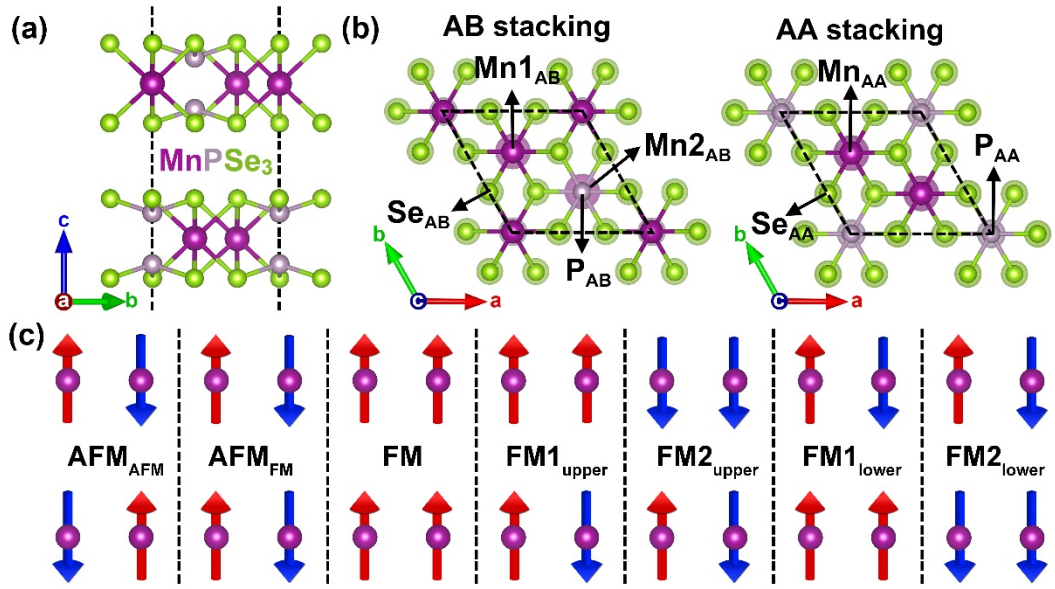

Figure 1. (a) Geometric structure of pristine $MnPSe_3$ bilayer. The dashed line represents the boundary of the unit cell. (b) Positions of the intercalated proton in AB/AA-stacked $H_{1/4}MnPSe_3$. Atoms belonging to the lower layer are shown with a larger radius for clarity. (c) Seven possible magnetic configurations of H-intercalated $MnPSe_3$ bilayer. Color code: Mn = purple, P = light purple, Se = green.

Interestingly, for all H_xMnPSe_3 structures considered in this work a AFM-FM hetero-magnetic order is energetically favourable. In this the upper layer, where the proton is bonded to, presents a FM spin arrangement, while the lower layer remains AFM, offering the opportunity to tune the magnetic order by controlling the position of the intercalated H, as we will discuss later. Taking $H_{1/4}MnPSe_3$ as an example, our calculation reveals that the structure favors a $FM2_{upper}$ magnetic order with an AFM interlayer coupling. The spin density centers around the Mn atoms with a local magnetic moment of 4.5 and 4.6 μ_B for the upper and lower layer, respectively, suggesting the d^5 high spin state of Mn atoms.[42] The nearest-neighboring Mn-Mn exchange parameters, J, are then estimated by mapping the total energies of proton intercalated $MnPSe_3$ in different magnetic configurations onto an Ising model (see Supporting Information – SI - for more details). As shown

in Table S1, the J in the upper (lower) layer, J_{upper}, (J_{lower}) is positive (negative) in all H_xMnPSe_3 structures, reflecting their AFM-FM hetero-magnetic ground states. We find J_{upper} and the interlayer exchange, J_{inter}, of $H_{1/4}MnPSe_3$ to be 2.53 meV and -0.32 meV, respectively, much higher than those of the pristine $MnPSe_3$ bilayer (-0.95 meV and -0.03 meV for J_{upper} and J_{inter}, respectively). Both J_{upper} and J_{inter} are sensitive to the concentration of the intercalated H, x. They both decrease with the decreasing x, making it possible to manipulate the strength of the magnetic interaction by controlling the concentration of the intercalated protons. In contrast, J_{lower} is less sensitive to x and remains close to the value of the pristine $MnPSe_3$ bilayer. This demonstrates that proton intercalation mainly tunes the magnetic properties of the layer where proton is bonded to.

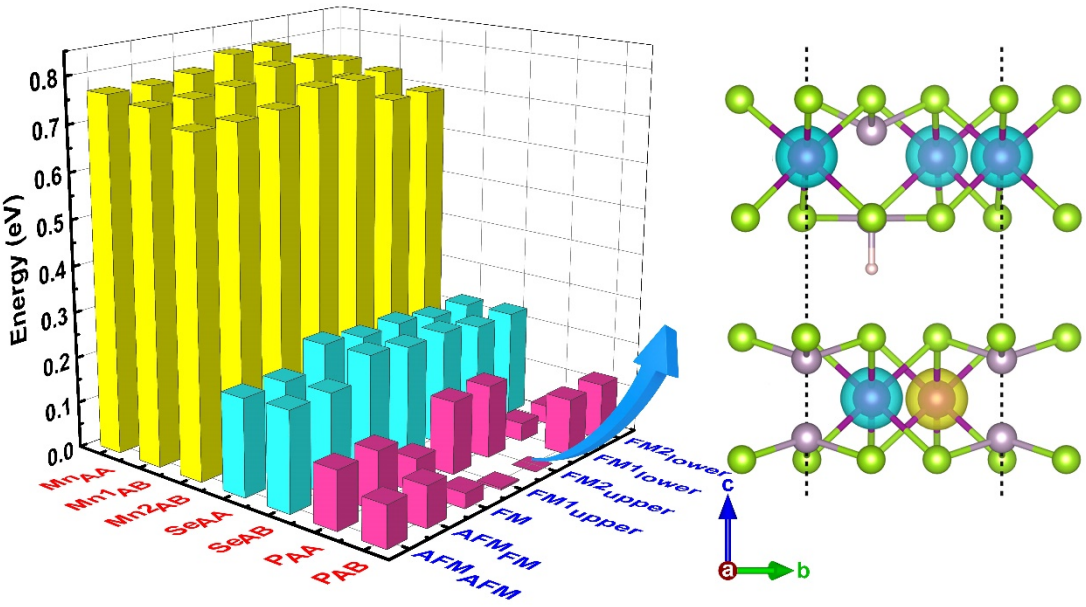

Figure 2. Energy map of $H_{1/4}MnPSe_3$ in different geometric and magnetic configurations. The lowest-energy structure together with the spin density distribution is shown in the right panel. The isosurface value is set to 0.04 electrons per $Å^3$. The yellow and cyan isosurface represents the spin-up and spin-down densities, respectively.

We then explore the electronic structures of proton intercalated $MnPSe_3$ by using the HSE06

functional. As shown in Figure 3a, the lower layer of $H_{1/4}MnPSe_3$ remains semiconductive, with a direct bandgap of 2.54 eV, which is close to that of pristine $MnPSe_3$ bilayer (2.56 eV). Notably, the upper layer displays robust half-metallicity, with a metallic spin-down channel where the Fermi level shifts into the valence bands, while the other spin channel shows a large bandgap of 2.32 eV. Our projected density of states (pDOS) shows that the metallic states near to the Fermi level are mainly contributed by the partially empty Mn e_g and Se p orbitals. The metallic states exhibit a delocalized spatial charge distribution (see Figure S4), suggesting that the spin-polarized charge carriers are itinerant in the entire basal plane of the H-bonded side. The half-metallicity induced by the intercalated proton is found for all H_xMnPSe_3 considered in this work (see Figure S5), suggesting its robustness against the variation of the intercalation level.

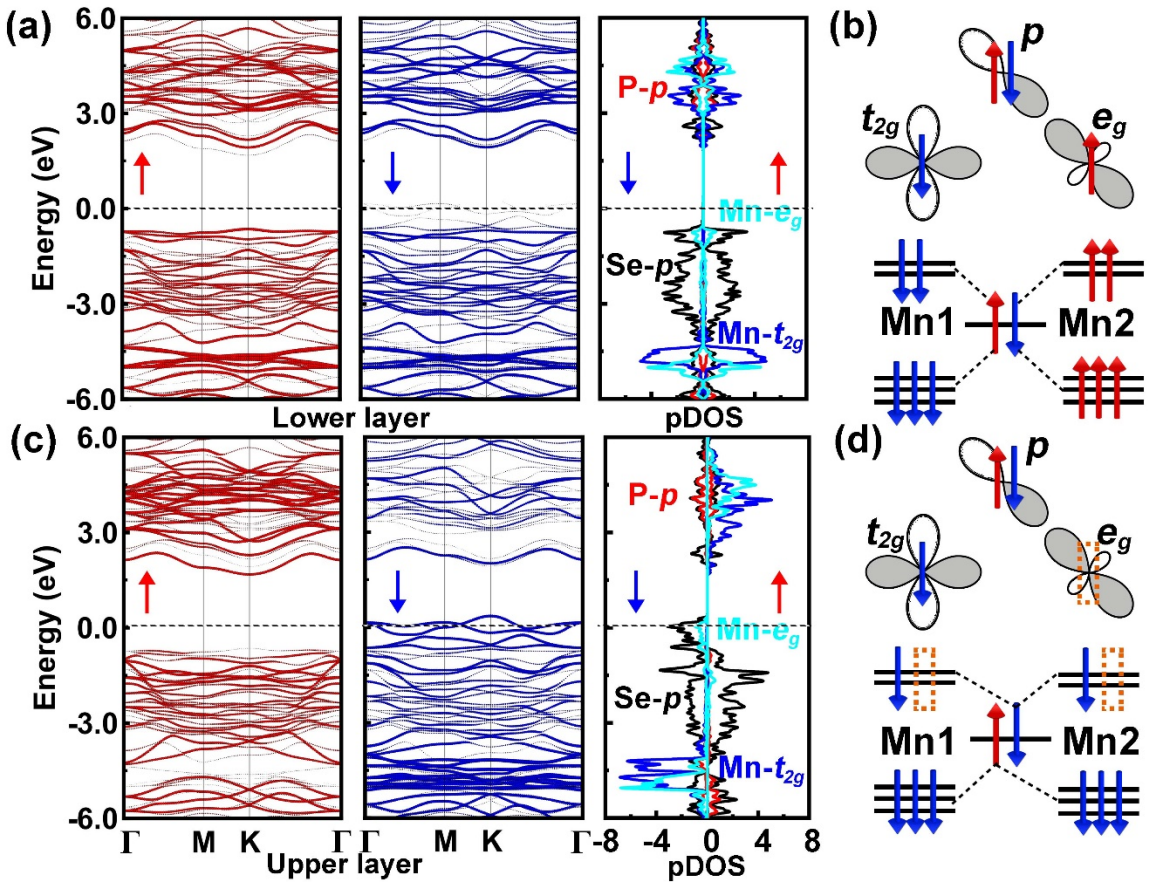

Figure 3. (a) and (c) The projected band structures and density of states for lower and upper layers of $H_{1/4}MnPSe_3$, respectively. The red and blue colors represent the spin-up and spin-down channels,

respectively. The Fermi level is marked by dashed lines. (b) and (d) The schematic representations of the superexchange interaction between two nearest Mn atoms in intact/pristine and H-bonded $MnPSe_3$ layer, respectively. The orange dashed rectangles indicate the partially empty e_g orbitals

It is of interest to understand the origin of the AFM to FM transition observed in the H-bonded $MnPSe_3$ layer. In $MnPSe_3$ the *d* orbital of Mn split into the threefold t_{2g} and twofold e_g manifolds under the octahedral ligand field,[43] a feature also confirmed by our orbital-resolved band structures (see Figure S6 and S7). The nearest Mn1 and Mn2 atoms are connected through an intermediate Se atom with Mn1-Se-Mn2 angle less than 90°, allowing a t_{2g}-*p*-e_g superexchange interaction. In pristine $MnPSe_3$ monolayer, both the t_{2g} and e_g orbitals are half-filled and the t_{2g}-*p*-e_g superexchange will be antiferromagnetic according to the Goodenough-Kanamori-Anderson rule.[44-46] This leads to a Neel-type AFM spin arrangement. Our charge density difference analysis (see Figure S8) indicates that the intercalated proton serves as hole donor, resulting in partially empty Mn e_g orbitals near to the Fermi level. The charge redistribution is spatially restricted to the monolayer where the proton is bonded due to the small atomic radii of H. In such case, the spin-up electrons from the *p* orbitals can form π bonds with the t_{2g} states of Mn1, while the remaining spin-down electrons in the *p* orbitals can hop into the partially empty e_g orbitals of Mn2 via σ bonds, leading to a FM superexchange interaction. Based on Hund's rule, the electrons in the *d* orbitals of Mn2 will exchange ferromagnetically thus the spin arrangement in the H-bonded layer will be ferromagnetic.

The biased proton position and the different magnetic orders in the upper and lower layers break the out-of-plane centrosymmetry, hence a ferroelectric polarization (*P*) can be expected in H_xMnPSe_3. The magnitude of *P* can be computed by directly integrating the local electron density with the out-of-plane coordinate over the entire supercell.[47, 48] In this way *P* is calculated to be 0.05, 0.02, 0.01 D/f.u. (f.u. = formula unit) for $H_{1/4}MnPSe_3$, $H_{1/8}MnPSe_3$, and $H_{1/12}MnPSe_3$, respectively.

Furthermore, P points from the H-bonded side to the pristine side. Our AIMD simulations of 10 ps at 300 K (Figure S9) show that there is no intercalated proton migrating between the two layers, suggesting the robustness of the polarized states against thermal fluctuations.[19] The three-step kinetic pathway for the polarization reversal is then revealed by using the climbing image nudged elastic band (cNEB) method. Firstly, the upper layer translates along the arm-chair direction, leading the system into a metastable AA-stacking phase. Then, the intercalated proton flips from the upper side to the lower side, followed by another interlayer translation, which reverses the first step. The overall activation barriers for the polarization reversal process are as low as 118, 61, and 45 meV/f.u. for $H_{1/4}MnPSe_3$, $H_{1/8}MnPSe_3$, and $H_{1/12}MnPSe_3$, respectively, values that are comparable to those of widely studied ferroelectrics like $PbTiO_3$, $BaTiO_3$ and 2D In_2Se_3.[47, 49, 50] This suggests the high feasibility of reversing the electric dipole moments in H_xMnPSe_3.

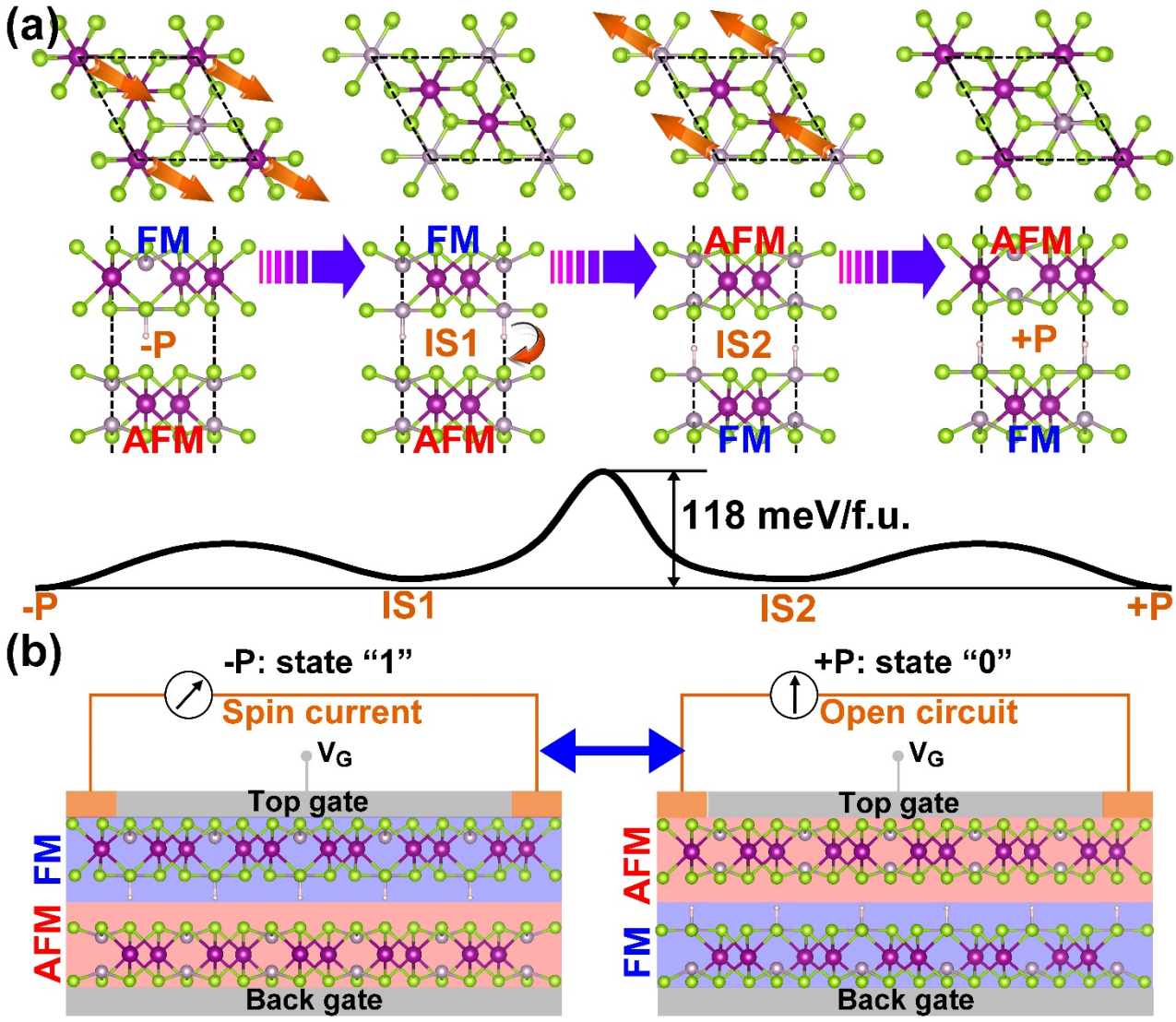

Figure 4. (a) The energy profile of the three-step pathway needed to reverse the spontaneous polarization of $H_{1/4}MnPSe_3$. The insets are the top and side views of the -P state, two intermediate states (IS1 and IS2), and +P state. The orange arrows represent the movements of the atoms involved. (b) A model of H_xMnPSe_3 based memory, where the logic states are stored in the bistable ferroelectric states, which can be read by checking the spin current or the magnetic order of the top layer.

So far, we have confirmed that H_xMnPSe_3 is a multiferroic material with FM-AFM hybrid magnetic order and out-of-plane ferroelectricity. Upon polarization reversal the position of the intercalated proton can be switched between the upper and the lower layer. Since the FM order and

half-metallicity exists only in the proton-bonded side of the bilayer, the magnetic order and electroconductivity of an individual layer can be explicitly tuned via FE switching. By taking $H_{1/4}MnPSe_3$ as an example, the upper layer of the -P phase is FM and half-metallic, while, through a FE switching, it becomes AFM and semiconductive in the equivalent +P phase due to the proton detachment. Notably, the FM/AFM and half-metallic/semiconductive transition are nonvolatile, which is a situation different from the FM to AFM transition in CrI_3 bilayers[12, 13] or the half-metallicity in VSe_2,[15] where a gate voltage is always required. The novel magnetoelectric coupling of H_xMnPSe_3 may facilitate the development of next-generation spintronics devices such as nonvolatile multiferroic memories. As shown in Figure 4b, the logic states can be stored in the +P and -P phases of H_xMnPSe_3 and the data writing can be finalized by switching the polarized states. The data can then be read through the magnetic signal of an individual layer detected by magneto-optical Kerr effect,[13] or more conveniently, by a spin current.

Two aspects are crucial in designing such hetero-magnetic multiferroics via intercalation. Firstly, the intercalated species shall be small, so that it can display a distinct vertical location in the van der Waals interspace. This will introduce ferroelectricity and more importantly, only modulate the magnetism of the layer to which they contact. Secondly, the host bilayers should be magnetic and the magnetic order of each layer should be tunable by elemental or charge doping. In this situation the attachment or detachment of intercalants can control the spin arrangement of the layer. Experimentally, various species, including ions and molecules, can be inserted into the weakly bonded layers, offering rich choices for suitable intercalants. Together with the expanding family of van der Waals 2D magnets, it is expected that more hetero-magnetic multiferroics with strong magnetoelectric coupling may be found.

In conclusion, we have introduced a hetero-magnetic multiferroic structural design to realize

nonvolatile ferroelectricity-controlled magnetic order and conductivity. As we have demonstrated in the case of multiferroic H_xMnPSe_3, the intercalated proton alters the magnetic order and conductivity of the layer it binds to via tuning the superexchange interaction and Fermi level. The vertical location of the proton can be controlled by the ferroelectric switching at a low energy cost, which consequently enables a ferroelectricity-controlled FM/AFM and half-metallic/semiconducting transition. Our results indicate a novel way for realizing ferroelectricity-tuned magnetic order and half-metallicity in a single multiferroic material, which shows promising applications in future magnetoelectric-coupled nanodevices such as electrically writen and magnetically read memories.

Acknowledgments

We acknowledge generous grants of high-performance computing resources provided by NCI National Facility and the Pawsey Supercomputing Centre through the National Computational Merit Allocation Scheme supported by the Australian Government and the Government of Western Australia. A. D. also greatly appreciates the financial support of the Australian Research Council under Discovery Project DP170103598, DP210100721, and DP210100331). SS acknowledge financial support from the Irish Research Council [IR- CLA/2019/127].

References

1. Burch, K. S.; Mandrus, D.; Park, J.-G. Magnetism in Two-Dimensional Van Der Waals Materials. *Nature* **2018,** 563 (7729), 47-52.

2. Huang, B.; Clark, G.; Navarro-Moratalla, E.; Klein, D. R.; Cheng, R.; Seyler, K. L.; Zhong, D.; Schmidgall, E.; McGuire, M. A.; Cobden, D. H.; Yao, W.; Xiao, D.; Jarillo-Herrero, P.; Xu, X. Layer-Dependent Ferromagnetism in a Van Der Waals Crystal Down to the Monolayer Limit. *Nature* **2017,** 546 (7657), 270-273.

3. Gong, C.; Li, L.; Li, Z.; Ji, H.; Stern, A.; Xia, Y.; Cao, T.; Bao, W.; Wang, C.; Wang, Y.; Qiu, Z. Q.; Cava, R. J.; Louie, S. G.; Xia, J.; Zhang, X. Discovery of Intrinsic Ferromagnetism in Two-Dimensional Van Der Waals Crystals. *Nature* **2017,** 546 (7657), 265-269.

4. Williams, T. J.; Aczel, A. A.; Lumsden, M. D.; Nagler, S. E.; Stone, M. B.; Yan, J. Q.; Mandrus, D. Magnetic Correlations in the Quasi-Two-Dimensional Semiconducting Ferromagnet Crsite3. *Phys. Rev. B* **2015,** 92 (14), 144404.

5. Bonilla, M.; Kolekar, S.; Ma, Y.; Diaz, H. C.; Kalappattil, V.; Das, R.; Eggers, T.; Gutierrez, H. R.; Phan, M.-H.;

Batzill, M. Strong Room-Temperature Ferromagnetism in Vse2 Monolayers on Van Der Waals Substrates. *Nat. Nanotechnol.* **2018,** 13 (4), 289-293.

6. O' Hara, D. J.; Zhu, T.; Trout, A. H.; Ahmed, A. S.; Luo, Y. K.; Lee, C. H.; Brenner, M. R.; Rajan, S.; Gupta, J. A.; McComb, D. W.; Kawakami, R. K. Room Temperature Intrinsic Ferromagnetism in Epitaxial Manganese Selenide Films in the Monolayer Limit. *Nano Lett.* **2018,** 18 (5), 3125-3131.

7. Ni, Z.; Haglund, A. V.; Wang, H.; Xu, B.; Bernhard, C.; Mandrus, D. G.; Qian, X.; Mele, E. J.; Kane, C. L.; Wu, L. Imaging the Néel Vector Switching in the Monolayer Antiferromagnet Mnpse3 with Strain-Controlled Ising Order. *Nat. Nanotechnol.* **2021**.

8. Webster, L.; Yan, J.-A. Strain-Tunable Magnetic Anisotropy in Monolayer $Crcl_3$, $Crbr_3$, and Cri_3. *Phys. Rev. B* **2018,** 98 (14), 144411.

9. Li, T.; Jiang, S.; Sivadas, N.; Wang, Z.; Xu, Y.; Weber, D.; Goldberger, J. E.; Watanabe, K.; Taniguchi, T.; Fennie, C. J.; Fai Mak, K.; Shan, J. Pressure-Controlled Interlayer Magnetism in Atomically Thin Cri3. *Nat. Mater.* **2019,** 18 (12), 1303-1308.

10. Afanasiev, D.; Hortensius, J. R.; Matthiesen, M.; Mañas-Valero, S.; Šiškins, M.; Lee, M.; Lesne, E.; van der Zant, H. S. J.; Steeneken, P. G.; Ivanov, B. A.; Coronado, E.; Caviglia, A. D. Controlling the Anisotropy of a Van Der Waals Antiferromagnet with Light. *Sci. Adv.* **2021,** 7 (23), eabf3096.

11. Jiang, S.; Li, L.; Wang, Z.; Mak, K. F.; Shan, J. Controlling Magnetism in 2d Cri3 by Electrostatic Doping. *Nat. Nanotechnol.* **2018,** 13 (7), 549-553.

12. Jiang, S.; Shan, J.; Mak, K. F. Electric-Field Switching of Two-Dimensional Van Der Waals Magnets. *Nat. Mater.* **2018,** 17 (5), 406-410.

13. Huang, B.; Clark, G.; Klein, D. R.; MacNeill, D.; Navarro-Moratalla, E.; Seyler, K. L.; Wilson, N.; McGuire, M. A.; Cobden, D. H.; Xiao, D.; Yao, W.; Jarillo-Herrero, P.; Xu, X. Electrical Control of 2d Magnetism in Bilayer Cri3. *Nat. Nanotechnol.* **2018,** 13 (7), 544-548.

14. Filianina, M.; Hanke, J.-P.; Lee, K.; Han, D.-S.; Jaiswal, S.; Rajan, A.; Jakob, G.; Mokrousov, Y.; Kläui, M. Electric-Field Control of Spin-Orbit Torques in Perpendicularly Magnetized W/Cofeb/Mgo Films. *Phys. Rev. Lett.* **2020,** 124 (21), 217701.

15. Gong, S.-J.; Gong, C.; Sun, Y.-Y.; Tong, W.-Y.; Duan, C.-G.; Chu, J.-H.; Zhang, X. Electrically Induced 2d Half-Metallic Antiferromagnets and Spin Field Effect Transistors. *Proc. Natl. Acad. Sci. U.S.A.* **2018,** 115 (34), 8511-8516.

16. Matsukura, F.; Tokura, Y.; Ohno, H. Control of Magnetism by Electric Fields. *Nat. Nanotechnol.* **2015,** 10 (3), 209-220.

17. Zhao, Y.; Zhang, J.-J.; Yuan, S.; Chen, Z. Nonvolatile Electrical Control and Heterointerface-Induced Half-Metallicity of 2d Ferromagnets. *Adv. Funct. Mater.* **2019,** 29 (24), 1901420.

18. Hill, N. A. Why Are There So Few Magnetic Ferroelectrics? *J. Phys. Chem. B* **2000,** 104 (29), 6694-6709.

19. Zhao, Y.; Lin, L.; Zhou, Q.; Li, Y.; Yuan, S.; Chen, Q.; Dong, S.; Wang, J. Surface Vacancy-Induced Switchable Electric Polarization and Enhanced Ferromagnetism in Monolayer Metal Trihalides. *Nano Lett.* **2018,** 18 (5), 2943-2949.

20. Huang, C.; Du, Y.; Wu, H.; Xiang, H.; Deng, K.; Kan, E. Prediction of Intrinsic Ferromagnetic Ferroelectricity in a Transition-Metal Halide Monolayer. *Phys. Rev. Lett.* **2018,** 120 (14), 147601.

21. Zhang, J.-J.; Lin, L.; Zhang, Y.; Wu, M.; Yakobson, B. I.; Dong, S. Type-Ii Multiferroic Hf2vc2f2 Mxene Monolayer with High Transition Temperature. *J. Am. Chem. Soc.* **2018,** 140 (30), 9768-9773.

22. Liu, X.; Wang, B.; Huang, X.; Dong, X.; Ren, Y.; Zhao, H.; Long, L.; Zheng, L. Room-Temperature Magnetoelectric Coupling in Electronic Ferroelectric Film Based on $[(N\text{-}C_3h_7)_4n][Fe^{iii}fe^{ii}(Dto)_3]$ (Dto = $C_2o_2s_2$). *J. Am. Chem. Soc.* **2021,** 143 (15), 5779-5785.

23. Li, L.; Wu, M.; Zeng, X. C. Facile and Versatile Functionalization of Two-Dimensional Carbon Nitrides by Design: Magnetism/Multiferroicity, Valleytronics, and Photovoltaics. **2019,** 29 (43), 1905752.

24. Tang, X.; Kou, L. Two-Dimensional Ferroics and Multiferroics: Platforms for New Physics and Applications. *J. Phys. Chem. Lett.* **2019,** 10 (21), 6634-6649.
25. Zhao, X.; Song, P.; Wang, C.; Riis-Jensen, A. C.; Fu, W.; Deng, Y.; Wan, D.; Kang, L.; Ning, S.; Dan, J.; Venkatesan, T.; Liu, Z.; Zhou, W.; Thygesen, K. S.; Luo, X.; Pennycook, S. J.; Loh, K. P. Engineering Covalently Bonded 2d Layered Materials by Self-Intercalation. *Nature* **2020,** 581 (7807), 171-177.
26. Lasek, K.; Coelho, P. M.; Zberecki, K.; Xin, Y.; Kolekar, S. K.; Li, J.; Batzill, M. Molecular Beam Epitaxy of Transition Metal (Ti-, V-, and Cr-) Tellurides: From Monolayer Ditellurides to Multilayer Self-Intercalation Compounds. *ACS Nano* **2020,** 14 (7), 8473-8484.
27. Hu, Y.; Yin, Y.; Li, S.; Zhou, H.; Li, D.; Zhang, G. Three-Fold Enhancement of in-Plane Thermal Conductivity of Borophene through Metallic Atom Intercalation. *Nano Lett.* **2020,** 20 (10), 7619-7626.
28. Banda, H.; Dou, J.-H.; Chen, T.; Libretto, N. J.; Chaudhary, M.; Bernard, G. M.; Miller, J. T.; Michaelis, V. K.; Dincă, M. High-Capacitance Pseudocapacitors from Li+ Ion Intercalation in Nonporous, Electrically Conductive 2d Coordination Polymers. *J. Am. Chem. Soc.* **2021,** 143 (5), 2285-2292.
29. Gong, Y.; Yuan, H.; Wu, C.-L.; Tang, P.; Yang, S.-Z.; Yang, A.; Li, G.; Liu, B.; van de Groep, J.; Brongersma, M. L.; Chisholm, M. F.; Zhang, S.-C.; Zhou, W.; Cui, Y. Spatially Controlled Doping of Two-Dimensional Sns2 through Intercalation for Electronics. *Nat. Nanotechnol.* **2018,** 13 (4), 294-299.
30. Zheng, G.; Xie, W.-Q.; Albarakati, S.; Algarni, M.; Tan, C.; Wang, Y.; Peng, J.; Partridge, J.; Farrar, L.; Yi, J.; Xiong, Y.; Tian, M.; Zhao, Y.-J.; Wang, L. Gate-Tuned Interlayer Coupling in Van Der Waals Ferromagnet Fe_3gete_2 Nanoflakes. *Phys. Rev. Lett.* **2020,** 125 (4), 047202.
31. Kresse, G.; Furthmüller, J. Efficiency of Ab-Initio Total Energy Calculations for Metals and Semiconductors Using a Plane-Wave Basis Set. *Comput. Mater. Sci.* **1996,** 6 (1), 15-50.
32. Kresse, G.; Furthmüller, J. Efficient Iterative Schemes for Ab Initio Total-Energy Calculations Using a Plane-Wave Basis Set. *Phys. Rev. B* **1996,** 54 (16), 11169-11186.
33. Kresse, G.; Hafner, J. Ab Initio Molecular-Dynamics Simulation of the Liquid-Metal--Amorphous-Semiconductor Transition in Germanium. *Phys. Rev. B* **1994,** 49 (20), 14251-14269.
34. Kresse, G.; Joubert, D. From Ultrasoft Pseudopotentials to the Projector Augmented-Wave Method. *Phys. Rev. B* **1999,** 59 (3), 1758-1775.
35. Perdew, J. P.; Ernzerhof, M.; Burke, K. Rationale for Mixing Exact Exchange with Density Functional Approximations. *J. Chem. Phys.* **1996,** 105 (22), 9982-9985.
36. Perdew, J. P.; Burke, K.; Ernzerhof, M. Generalized Gradient Approximation Made Simple. *Phys. Rev. Lett.* **1996,** 77 (18), 3865.
37. Grimme, S. Semiempirical Gga-Type Density Functional Constructed with a Long-Range Dispersion Correction. *J. Comput. Chem.* **2006,** 27 (15), 1787-1799.
38. Li, X.; Cao, T.; Niu, Q.; Shi, J.; Feng, J. Coupling the Valley Degree of Freedom to Antiferromagnetic Order. **2013,** 110 (10), 3738-3742.
39. Krukau, A. V.; Vydrov, O. A.; Izmaylov, A. F.; Scuseria, G. E. Influence of the Exchange Screening Parameter on the Performance of Screened Hybrid Functionals. *J. Chem. Phys.* **2006,** 125 (22), 224106.
40. Mills, G.; Jónsson, H.; Schenter, G. K. Reversible Work Transition State Theory: Application to Dissociative Adsorption of Hydrogen. *Surf. Sci.* **1995,** 324 (2), 305-337.
41. Andersen, H. C. Molecular Dynamics Simulations at Constant Pressure and/or Temperature. *J. Chem. Phys.* **1980,** 72 (4), 2384-2393.
42. Sivadas, N.; Okamoto, S.; Xiao, D. Gate-Controllable Magneto-Optic Kerr Effect in Layered Collinear Antiferromagnets. *Phys. Rev. Lett.* **2016,** 117 (26), 267203.
43. Burns, R. G.; Burns, R. G., *Mineralogical Applications of Crystal Field Theory*. 2nd ed.; Cambridge university press: Cambridge, 1993.
44. Goodenough, J. B., *Magnetism and the Chemical Bond*. 1st ed.; John Wiley & Sons, Inc.: New York: London,

1963.
45. Goodenough, J. B.; Loeb, A. L. Theory of Ionic Ordering, Crystal Distortion, and Magnetic Exchange Due to Covalent Forces in Spinels. *Phys. Rev.* **1955,** 98 (2), 391-408.
46. Kanamori, J. Superexchange Interaction and Symmetry Properties of Electron Orbitals. *J. Phys. Chem. Solids* **1959,** 10 (2), 87-98.
47. Ding, W.; Zhu, J.; Wang, Z.; Gao, Y.; Xiao, D.; Gu, Y.; Zhang, Z.; Zhu, W. Prediction of Intrinsic Two-Dimensional Ferroelectrics in In2se3 and Other Iii2-Vi3 Van Der Waals Materials. *Nat. Commun.* **2017,** 8, 14956.
48. Zhang, L.; Tang, C.; Zhang, C.; Du, A. First-Principles Screening of Novel Ferroelectric Mxene Phases with a Large Piezoelectric Response and Unusual Auxeticity. *Nanoscale* **2020,** 12 (41), 21291-21298.
49. Cohen, R. E. Origin of Ferroelectricity in Perovskite Oxides. *Nature* **1992,** 358 (6382), 136-138.
50. Zhang, Y.; Sun, J.; Perdew, J. P.; Wu, X. Comparative First-Principles Studies of Prototypical Ferroelectric Materials by Lda, Gga, and Scan Meta-Gga. *Phys. Rev. B* **2017,** 96 (3), 035143.